Geophys. J. Int. (2001) **147,** 562–578

Glacial isostatic adjustment on a rotating earth

Jerry X. Mitrovica,[1] Glenn A. Milne,[2] and James L. Davis[3]

[1] *Department of Physics, University of Toronto,* 60 *St. George Street, Toronto, Ontario, Canada* M5S 1A7. *E-mail: jxm@physics.utoronto.ca*
[2] *Department of Geological Sciences, University of Durham, Science Labs, South Road, Durham,* DH1 3LE, *UK*
[3] *Harvard-Smithsonian Center for Astrophysics,* 60 *Garden Street,* MS42, *Cambridge,* MA 02138, *USA*

Accepted 2001 June 21. Received 2001 May 18; in original form 2000 July 28

SUMMARY

We extend and complete previous work to compute the influence of perturbations to the rotation vector on a suite of observables associated with glacial isostatic adjustment (GIA). We emphasize observables relevant to present and future geodetic missions (for example, present-day 3-D crustal motions, relative sea-level change and geoid or absolute sea-level variations). Our calculations adopt spherically symmetric, self-gravitating, Maxwell viscoelastic earth models while incorporating realistic mass (ice plus ocean) load and rotation variations. The predicted rotation-induced signals are dominated by the influence of true polar wander (TPW). The spatial geometry of the TPW-induced relative sea level, geoid and radial velocity fields is primarily that of a degree two, order one surface spherical harmonic. The spatial variation of the horizontal velocity vectors is given by the gradient of this harmonic. The peak radial and horizontal velocities are of the order of 0.5 mm yr^{-1}; however, we show that this value is sensitive to the adopted profile of mantle viscosity. We also demonstrate that an accurate prediction of TPW-induced sea level and 3-D crustal deformation rates requires that a realistic number of glacial cycles be incorporated into the ice load history. We conclude that geodetic observations of the GIA process should be analysed using a GIA theory valid for a rotating planet. Finally, we also consider variations in rotation driven by simple present-day polar melting scenarios and predict the influence of these variations on a suite of geophysical observables. We find that the rotational feedback associated with Greenland melting is capable of significantly perturbing both relative and absolute sea-level variations.

Key words: 3-D crustal deformations, Earth's rotation, geodesy, glacial rebound, sea level.

1 INTRODUCTION

Perturbations to the Earth's rotation vector associated with the glacial cycles of the Late Pleistocene, including both changes in the rotation rate and the wander of the rotation pole with respect to the surface geography, have been the focus of much activity (e.g. O'Connell 1971; Nakiboglua & Lambeck 1980; Sabadini & Peltier 1981; Sabadini *et al.* 1982, 1984; Yuen *et al.* 1982; Wu & Peltier 1984; Yuen & Sabadini 1985; Peltier 1988; Vermeersen & Sabadini 1996; Vermeersen *et al.* 1997, Mitrovica & Milne 1998; Johnston & Lambeck 1999). In general, the goals of these studies were to establish a theoretical methodology for making accurate predictions and/or to infer mantle rheology from observational constraints on secular changes in the rotation vector.

More recently, there has been growing appreciation that variations in the rotation vector due to glacial isostatic adjustment (henceforth 'GIA'), particularly true polar wander ('TPW'), can also feedback into other observables traditionally considered in GIA studies. The influence of TPW on sea-level variations is the prime example (e.g. Han & Wahr 1989; Bills & James 1996; Milne & Mitrovica 1996, 1998; Sabadini & Vermeersen 1997; Peltier 1998a,b,c, 1999). Indeed, Milne & Mitrovica (1996, 1998) have extended the traditional 'sea-level equation' governing gravitationally self-consistent GIA-induced sea-level variations on a viscoelastic, non-rotating planet (Farrell & Clark 1976) to include the effects of concomitant GIA-induced perturbations in the Earth's rotation vector.

The geometry of rotation-induced variations in sea-level is explored in Fig. 1. This geometry was first discussed by Han & Wahr (1989) in the context of GIA. It is also relevant to longer-timescale variations in Earth rotation such as mantle convection (Sabadini *et al.* 1990; Mound & Mitrovica 1998) or to shorter-timescale variations such as the annual and Chandler wobbles, which give rise to so-called pole tides (e.g. Miller & Wunsch 1973; Wahr 1985). The centrifugal potential associated

© 2001 RAS

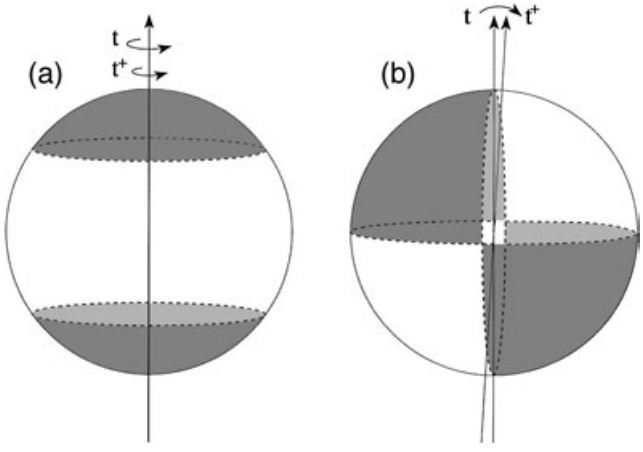

Figure 1. Spatial variation of the perturbation to the centrifugal potential associated with changes in (a) the magnitude and (b) the orientation of the Earth's rotation vector from time t to t^+. See text for a detailed discussion. The shaded regions indicate areas in which the potential perturbation has the same sign.

with Earth rotation has a geographically varying component governed by a spherical harmonic degree two and order zero form. Changes in the magnitude or orientation of the rotation vector act to produce a perturbation in this centrifugal potential that we will term the 'driving potential' or the 'rotational potential perturbation'. Perturbations in the rotation rate (Fig. 1a) produce a driving potential that may be expressed as a surface spherical harmonic of degree two and order zero (together with a degree zero term). The (2, 0) perturbation has a dependence on colatitude θ that is proportional to $(\cos^2\theta - 1/3)$ and thus the magnitude at the poles is twice that at the equator. The influence of TPW on the driving potential is more complicated (Fig. 1b), since in this case the forcing is the difference between two ellipsoidal forms whose axes are rotated relative to each other (clockwise in Fig. 1b). The driving potential is dominated (for small perturbations in the pole position) by a degree two and order one geometry, and therefore it is zero along two great circles. The first is 90° from the pole (that is, the equator at present day). The second is a great circle that includes the rotation pole and that is 90° from the great circle TPW path. This geometry produces the four quadrants shown in the figure, with antipolar quadrants showing the same sign of perturbation (as indicated in Fig. 1b). The maximum perturbation is at the centre of each quadrant.

The sea-level responses associated with perturbations in the rotation vector are dominated by TPW effects (e.g. Han & Wahr 1989; Sabadini *et al.* 1990; Milne & Mitrovica 1996; Mound & Mitrovica 1998). Accordingly, the geometry of this sea-level response has the form shown in Fig. 1(b). (Of course, the surface loading effects induced by the sea-level variations will introduce signals at higher degrees.) As an example, Milne & Mitrovica (1996, 1998) found that GIA-induced perturbations in the rotation vector are characterized by a TPW path that lies roughly along the 286°E/106°E lines of longitude over the last glacial cycle. (Relative to the north pole, this trajectory reflects a TPW path directly away from or towards north-eastern Canada. During the last glacial cycle, the displacement of the pole from its present position was found to be $\sim 0.1°$ for realistic viscosity profiles.) As a result, the relative sea-level (henceforth 'RSL', where we define RSL as the height of the geoid, or absolute sea level, relative to the solid surface) signals they predicted were close to zero along both the equator and the great circle associated with the 16°E/196°E lines of longitude. Furthermore, the maximum signals they obtained were found at mid-latitudes along the 286°E/106°E lines of longitude (the Great Lakes/US east coast, the southern tip of South America, southwestern Australia and central Asia). Milne & Mitrovica (1996, 1998) predicted present-day rates of RSL change of the order of 0.15 mm yr^{-1} at specific sites or 0.30 mm yr^{-1} peak-to-peak (that is, across two quadrants with signals of opposite sign; for example, the US east coast and either central Asia or southern Chile). Rotation-induced site-specific RSL variations were found to be non-monotonic in time since the last glacial maximum (LGM), with maximum peak-to-peak variations of the order of 15 m. These predictions were later confirmed by Peltier (1998a,b,c, 1999).

The TPW-induced driving potential shown in Fig. 1(b) can influence other geophysical observables associated with GIA. Sabadini *et al.* (1982) considered TPW-induced stresses within the lithosphere (see also Heiskanen & Vening Meinesz 1958). Furthermore, the study by Han & Wahr (1989) included predictions of both RSL and free-air gravity. More recently, Bills (1995) has pointed out that TPW driven by GIA 'causes vertical deflection in both the solid surface and the geoid', that is, the two bounding surfaces of RSL change. Indeed, Peltier (1997, 1999) has predicted the rotational effect on present-day rates of change in these global fields. He ultimately concluded that TPW would produce 'no substantial change in [the] amplitude' of the GIA-induced geoid anomaly, and that impending satellite measurements of absolute sea-level rise 'will not be significantly biased by the glacial isostatic adjustment effect' (Peltier 1999, p. 121).

In this study we revisit predictions found in previous studies and extend these predictions in several important ways. First, we investigate present-day 3-D (i.e. radial and horizontal) crustal deformation rates associated with GIA-induced TPW. Second, we explore the sensitivity of these GIA predictions, as well as predictions of RSL and absolute sea-level (geoid) anomalies, to variations in the mantle viscosity in order to derive bounds on the GIA signal associated with TPW 'feedback'. Finally, we complete the study by considering TPW effects arising from ongoing ice–ocean mass transfer. Geophysical observables linked to recent melting or growth of the major polar ice complexes (Antarctic, Greenland) and melting from mountain glaciers have been the source of active interest; however, the feedback of TPW into predictions of these observables has yet to be investigated. In the next section we review relevant background material and then turn, in the subsequent section, to the presentation of results.

2 BACKGROUND

Our numerical predictions adopt spherically symmetric, self-gravitating, viscoelastic earth models. The elastic structure of the earth model is given by the seismically inferred model PREM (Dziewonski & Anderson 1981).

The calculations are performed in several stages. First, the sea-level equation valid for a rotating earth (Milne & Mitrovica 1996, 1998) is solved for a specified ice history (see below) and earth model. Following Milne & Mitrovica (1996, 1998), we adopt the pseudospectral numerical algorithm (Mitrovica & Peltier 1991) for this purpose with a spherical harmonic

truncation at degree and order 128. The sea-level theory also requires a method for predicting GIA-induced perturbations to the rotation vector, and in this case we follow the approach outlined in Wu & Peltier (1984). Mitrovica & Milne (1998) have shown that this theory provides results that are essentially identical to an earlier theory by Sabadini *et al.* (1982) when the Chandler wobble is filtered from the latter (see also Vermeersen & Sabadini 1996).

The output of the sea-level equation includes gravitationally self-consistent variations in the rotation vector and ocean load due to the prescribed ice mass evolution. These outputs are then applied, in the second stage of the calculation, to predict a variety of geophysical observables. In this case, we adopt and extend spectral approaches described in previous GIA studies. Let us denote the radial displacement, horizontal (vector) displacement and geoid (absolute sea-level) anomalies by $R(\theta, \psi, t)$, $\mathbf{V}(\theta, \psi, t)$ and $G(\theta, \psi, t)$, respectively, where θ is the colatitude, ψ is the east longitude and t is time. We can represent these fields using spherical harmonic decompositions of the form

$$R(\theta, \psi, t) = \sum_{\ell=0}^{\infty} \sum_{m=-\ell}^{\ell} R_{\ell,m}(t)\, Y_{\ell,m}(\theta, \psi)\,, \tag{1}$$

$$\vec{\mathbf{V}}(\theta, \psi, t) = \sum_{\ell=0}^{\infty} \sum_{m=-\ell}^{\ell} V_{\ell,m}(t) \boldsymbol{\nabla} Y_{\ell,m}(\theta, \psi) \tag{2}$$

and

$$G(\theta, \psi, t) = \sum_{\ell=0}^{\infty} \sum_{m=-\ell}^{\ell} G_{\ell,m}(t)\, Y_{\ell,m}(\theta, \psi)\,, \tag{3}$$

where $\boldsymbol{\nabla}$ is the 2-D gradient operator and $Y_{1,m}$ is the surface spherical harmonic at degree l and order m. We adopt the following normalization,

$$\iint_{\Omega} Y^{\dagger}_{\ell',m'}(\theta, \psi)\, Y_{\ell,m}(\theta, \psi) \sin\theta\, d\theta d\psi = 4\pi \delta_{\ell',\ell} \delta_{m',m}\,, \tag{4}$$

for this decomposition, where † denotes the complex conjugate and the subscript Ω denotes integration over the unit sphere.

Let us next denote the spherical harmonic coefficients of the total surface mass (ice plus ocean) load and the perturbing rotational potential by $L_{l,m}$ and $\Lambda_{l,m}$, respectively. The harmonic coefficients in eqs (1)–(3) are then given by (Mitrovica & Peltier 1991; Mitrovica *et al.* 1994a; Milne & Mitrovica 1996, 1998)

$$R_{\ell,m}(t) = \int_{-\infty}^{t} \left[\frac{\Lambda_{\ell,m}(t')}{g}\, \Gamma^{\mathrm{T}}_{\ell}(t - t') + \frac{4\pi a^3}{(2\ell+1) M_{\mathrm{e}}}\, L_{\ell,m}(t') \Gamma^{\mathrm{L}}_{\ell}(t - t') \right] dt'\,, \tag{5}$$

$$V_{\ell,m}(t) = \int_{-\infty}^{t} \left[\frac{\Lambda_{\ell,m}(t')}{g}\, \Upsilon^{\mathrm{T}}_{\ell}(t - t') + \frac{4\pi a^3}{(2\ell+1) M_{\mathrm{e}}}\, L_{\ell,m}(t') \Upsilon^{\mathrm{L}}_{\ell}(t - t') \right] dt' \tag{6}$$

and

$$G_{\ell,m}(t) = \int_{-\infty}^{t} \left[\frac{\Lambda_{\ell,m}(t')}{g}\, \Phi^{\mathrm{T}}_{\ell}(t - t') + \frac{4\pi a^3}{(2\ell+1) M_{\mathrm{e}}} \times L_{\ell,m}(t') \Phi^{\mathrm{L}}_{\ell}(t - t') \right] dt' + \frac{\Delta\Phi(t)}{g}\, \delta_{\ell,0} \delta_{m,0}\,, \tag{7}$$

where a, M_{e} and g are the Earth's radius, mass and surface gravitational acceleration, respectively. The term $\Delta\Phi(t)/g$ in eq. (7) is a uniform shift in the geoid (or absolute sea level) that is constrained by conserving the mass of the total surface load.

The degree- and time-dependent forms Γ^{T}, Γ^{L}, Υ^{T}, Υ^{L}, Φ^{T} and Φ^{L} incorporate the viscoelastic structure of the earth model and they are constructed by combining surface load and tidal-effective Love number parameters. Explicit expressions for these forms are provided in the Appendix.

We define relative sea level as the level of the sea surface or geoid relative to the solid surface. Accordingly, the RSL anomaly, $S(\theta, \psi, t)$, can expressed in terms of perturbations to these two bounding surfaces as (e.g. Mitrovica & Peltier 1991)

$$S(\theta, \psi, t) = \sum_{\ell=0}^{\infty} \sum_{m=-\ell}^{\ell} [G_{\ell,m}(t) - R_{\ell,m}(t)]\, Y_{\ell,m}(\theta, \psi)\,. \tag{8}$$

The driving potential Λ can be expressed in terms of the perturbations to the components of the Earth's rotation vector. Let us denote a right-handed Cartesian coordinate system by (x_i), with the origin of this system taken to be the centre of mass of the earth model in its unperturbed state. We orient this system so that the x_1 axis is aligned with the Greenwich longitude and the x_2 axis is 90°E of x_1. Prior to surface loading, the rotation vector, $\boldsymbol{\omega}(t)$, is assumed to be $(0, 0, \Omega)$. Subsequently, the components ω_i $(i = 1, 2)$ generally become non-zero, and the ω_i are conventionally written in the form (e.g. Munk & MacDonald 1960)

$$\omega_i(t) = \Omega(\delta_{i3} + m_i(t))\,. \tag{9}$$

In this case, the perturbation to the rotational potential from the equilibrium value can then be written as (e.g. Lambeck 1980; Milne & Mitrovica 1996, 1998)

$$\Lambda(\theta, \psi, t) = \Lambda_{0,0}(t)\, Y_{0,0}(\theta, \psi) + \sum_{m=-2}^{2} \Lambda_{2,m}(t)\, Y_{2,m}(\theta, \psi)\,, \tag{10}$$

where

$$\Lambda_{0,0}(t) = \frac{a^2\Omega^2}{3}\, [m^2(t) + 2m_3(t)]\,, \tag{11a}$$

$$\Lambda_{2,0}(t) = \frac{a^2\Omega^2}{6\sqrt{5}}\, [m_1^2(t) + m_2^2(t) - 2m_3^2(t) - 4m_3(t)]\,, \tag{11b}$$

$$\Lambda_{2,1}(t) = \frac{a^2\Omega^2}{\sqrt{30}}\, [m_1(t)(1 + m_3(t)) - i m_2(t)(1 + m_3(t))]\,, \tag{11c}$$

$$\Lambda_{2,2}(t) = \frac{a^2\Omega^2}{\sqrt{5}\sqrt{24}}\, [(m_2^2(t) - m_1^2(t)) + i 2 m_1(t) m_2(t)]\,, \tag{11d}$$

with

$$\Lambda_{2,-m} = (-1)^m \Lambda^{\dagger}_{2,m}\,. \tag{11e}$$

The symbol i is the complex number $\sqrt{-1}$.

In the results presented below we will generally focus on present-day *rates of change* of the various geophysical observables discussed above. In this regard, predictions of 3-D crustal deformation rates $(\dot{R}, \dot{\mathbf{V}})$ will be presented in a local Cartesian coordinate system in which $\dot{V}_\theta$ and $\dot{V}_\phi$ denote local south and east components of the horizontal velocities, respectively, and $\dot{R}$ is the upward component of the velocity.

We have found that the 'rotational effect' on the geophysical observables described below is dominated by TPW. Although the contributions to these predictions arising from changes in the rotation rate are small, we emphasize that the theory adopted for the predictions incorporates the total perturbation to the rotation vector.

As discussed above, we will consider TPW-induced signals associated with both the Late Pleistocene glacial cycles and ongoing ice–ocean mass transfer. The former calculations will most commonly be based on a 'test' earth model characterized by a very high-viscosity (effectively elastic) lithospheric lid of thickness 95 km, an upper mantle viscosity of 10^{21} Pa s and a lower mantle viscosity of 2×10^{21} Pa s. We also perform a sensitivity analysis by considering a suite of predictions in which the lower mantle viscosity (denoted by $\nu_{\rm lm}$) is varied over several orders of magnitude. These predictions also adopt the ICE-3G model for the most recent deglaciation event (Tushingham & Peltier 1991). The model is adapted, by reversing the sign of the ICE-3G ice load increments and spacing them backwards in time, to include a glacial cycle of duration 100 kyr. Furthermore, our numerical predictions generally include eight such cycles, beginning at 805 ka and ending (as in ICE-3G) at 5 ka.

Since the present-day mass balance of the Antarctic and Greenland ice complexes is uncertain, the second part of our study, dealing with ongoing ice–ocean mass transfer, is based on simple melting scenarios in which the change in the ice load is assumed to be uniform over these two regions. As an illustration, we consider the case in which the equivalent of 1 mm $\rm yr^{-1}$ of eustatic sea level is removed from each of these ice sheets; the response associated with any other amplitude, including a growth of the ice sheets, can be determined by simply scaling this test case. We also consider TPW-induced feedback arising from the melting of mountain glaciers as tabulated by Meier (1984). The response of the Earth to these relatively short-timescale melting events is essentially elastic and our predictions are therefore independent of the assumed (and uncertain) mantle viscosity profile and lithospheric thickness.

3 RESULTS AND DISCUSSION

3.1 Rotational feedback on GIA: Late Pleistocene glacial cycles

We show, in Figs 2 and 3, the TPW path predicted using the 'test' viscoelastic earth model described above and the revised ICE-3G ice history. In both of these plots, X and Y refer to coordinate axes aligned in the direction of Greenwich and 90°E longitude, respectively (axes x_1 and x_2, as defined above). Fig. 2 illustrates the spatial geometry of the GIA-induced TPW. The pole position at the onset of glaciation coincides with the origin of the plot. In accord with Milne & Mitrovica (1996, 1998), the TPW path lies roughly along the 286°E/106°E lines of longitude. Within each glaciation phase, the pole moves away from Hudson Bay (that is, the location of the massive Laurentide ice complex) and the pole path reverses during the subsequent deglaciation. The bobbing of the pole is accompanied by a drift such that by the last glacial maximum (LGM) the pole is predicted to have moved away from northeastern Canada a total angular distance of $\sim 0.25°$. Furthermore, a residual pole displacement (denoted by the solid dot) of $\sim 0.17°$ is predicted

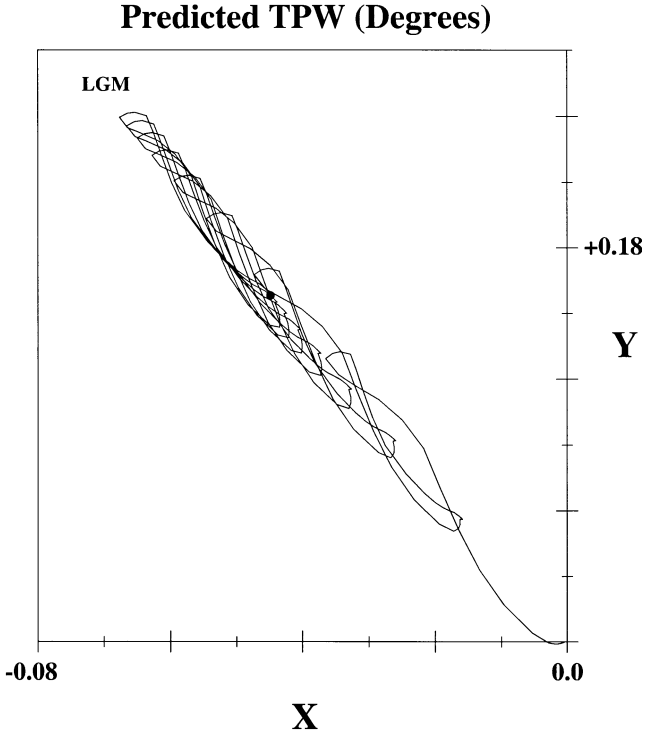

Figure 2. Predicted TPW path over a period extending from the onset of glaciation (the origin of the plot) through eight glacial cycles. At last glacial maximum (LGM) the pole position reaches the top-left portion of the plot, while the predicted present-day pole position is denoted by the solid dot near the centre of the plot. The prediction is based on the earth model and ice history described in the text. The coordinate axes are aligned in the direction of Greenwich (X) and 90°E longitude (Y).

at present day. The cyclic nature of the TPW is also clearly evident in Fig. 3, where both the X and Y coordinates of pole position reflect the presence of the eight model glacial cycles. The predicted long-term drift in the pole position reaches roughly a steady state by the most recent cycles of the ice history. Predictions of TPW over multiple glacial cycles have also recently been considered by Sabadini & Vermeersen (1997).

3.1.1 Relative sea level

TPW-induced effects on RSL were described in detail by Milne & Mitrovica (1996, 1998) and we therefore only provide a cursory review here in support of later discussion. In Fig. 4 we show a global map of the present-day rate of change of sea level predicted for the cases in which the rotational perturbation is (a) neglected and (c) included, as well as for (b) the difference in these two cases (see also Peltier 1998a,b,c, 1999).

In the near field of the Late Pleistocene ice sheets (i.e. the polar regions), predictions of relative sea-level change (Figs 4a and c) are dominated by the radial response of the solid surface to the most recent deglaciation. In particular, regions once covered by ice are now rebounding (at rates that exceed 10 mm $\rm yr^{-1}$ in Hudson Bay and Fennoscandia, for example) and this rebound gives rise to a notable RSL fall. In the periphery of the rebound centres, the bulges encircling the now disintegrated ice complexes are presently subsiding and this subsidence produces an RSL rise (which can reach as high as 5 mm $\rm yr^{-1}$). In the far field, the sea-level predictions show two main effects. Regions in the vicinity of continent margins

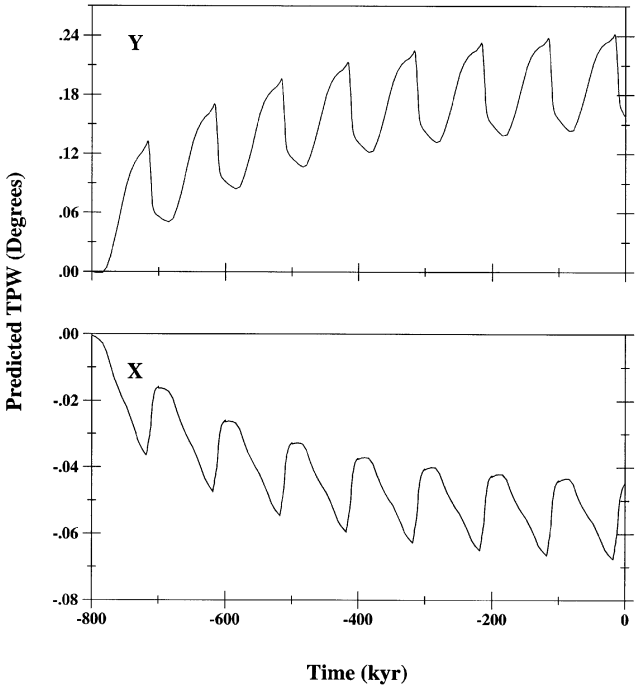

Figure 3. Predicted TPW path as a function of time from the onset of glaciation to the present day. The prediction is based on the earth model and ice history described in the text. The two frames provide components of the TPW in the direction of Greenwich (X) and 90°E longitude (Y).

are commonly characterized by an offshore sea-level rise and an onshore region of anomalously high sea-level fall. This pattern reflects the flexure or 'levering' (hence the term 'continental levering') of the lithosphere due to ocean loading (e.g. Clark *et al.* 1978; Nakada & Lambeck 1989). The ocean load in this region acts to deform the lithosphere downwards offshore and upwards onshore. In the case of Australia, the levering effect is sufficient to perturb the whole continent upwards. (The spatial extent of the levering is, not surprisingly, a strong function of the assumed lithospheric thickness.) The second far-field effect is a small, sub-1 mm yr^{-1}, RSL fall in regions away from continents. As discussed by Mitrovica & Peltier (1991), this signal originates in part from a broad subsidence of the geoid in the far field that is due to movement of ocean mass away from the far field into regions vacated by the subsiding peripheral bulges (see also Johnston 1993). This process has been termed 'ocean syphoning'. Ocean syphoning and continental levering do not act in isolation; syphoning acts in tandem with levering in the far-field.

Fig. 4(b) exhibits the characteristic degree two, order one form of the TPW-induced driving potential (Fig. 1b). TPW has a maximum site-specific effect of $\sim$0.13 mm yr^{-1} and a maximum peak-to-peak signal of $\sim$0.26 mm yr^{-1} on present-day RSL rates for our adopted ice and earth models. The amplitude of the TPW signal is such that RSL is predicted to be rising in North America. Milne & Mitrovica (1996, 1998) examined the dependence of this amplitude on variations in the earth model. The TPW-induced effect modulates the geometry of the predicted relative sea-level rates in the middle of each of the quadrants defining the driving potential (compare Figs 4a and c). As an example, the rotation-induced sea-level rise in Australia (Fig. 4b) acts to produce a more continuous and higher-amplitude band of sea-level rise offshore and a more subdued sea-level fall over the continent than was predicted in the non-rotating case.

In Fig. 5 we show predictions of the TPW feedback (i.e. rotating minus non-rotating predictions) on RSL curves at six widely distributed sites (dashed lines). Sites Clinton, Bahia Gente Grande, Tientsin and Perth are close to the middle of the $Y_{2,1}$ quadrants in Fig. 4(b), and the predicted signal is therefore highest at these locations. In contrast, Recife is near the equator and Bremerhaven is close to the great circle longitude of zero rotational potential (i.e. 90° from the pole path), hence the predicted signal at these sites is relatively small. Clinton and Perth are antipodal, as are Bahia Gente Grande and Tienstsin, thus the form of the TPW-induced RSL signal for each pair of sites is nearly identical.

Peltier (1998a,b,c, 1999) adopted essentially the same numerical formalism initially developed by Milne & Mitrovica (1996, 1998) with the exception that he advocated a form for the rotational potential (eqs 10 and 11) in which second-order terms were dropped. Neglecting terms containing products of m_1, m_2 and m_3, we derive

$$\Lambda_{0,0}(t) = \frac{2a^2\Omega^2}{3}\, m_3(t)\,, \tag{12a}$$

$$\Lambda_{2,0}(t) = \frac{-2a^2\Omega^2}{3\sqrt{5}}\, m_3(t)\,, \tag{12b}$$

$$\Lambda_{2,1}(t) = \frac{a^2\Omega^2}{\sqrt{30}}\, [m_1(t) - i m_2(t)]\,, \tag{12c}$$

$$\Lambda_{2,2}(t) = 0\,, \tag{12d}$$

with

$$\Lambda_{2,-1} = -\Lambda^{\dagger}_{2,1}\,. \tag{12e}$$

Peltier's (1998a,b,c, 1999) expressions for the rotational driving potential, based on the same approximation used to derive eqs (12a)–(12e), contain a sign error in the $\Lambda_{2,-1}$ term. In particular, in each of these publications he derives the following:

$$\Lambda_{2,-1} = \Lambda^{\dagger}_{2,1}\,. \tag{13}$$

The expression (12e), which is a special case of the more general relation (11e), is certainly the correct expression since it is required for any real-valued field $\Lambda(\theta, \psi)$.

The dotted lines in Fig. 5 verify that the *correct* first-order expressions for the rotational potential (eqs 12a–e) yield predictions that are indistinguishable from the exact expressions (11a–e) for the case of the relatively small (sub-1°) pole perturbations characteristic of GIA.

3.1.2 *Sea surface and sea bottom*

In this section we focus on vertical deformations of the two bounding surfaces of RSL, namely, the sea surface (alternatively, the geoid or absolute sea level), and the sea bottom (or solid surface). In Figs 6 and 7 we show results analogous to Fig. 4 with the exception that the fields are present-day vertical rates of change of the geoid and solid surface, respectively, due to the influence of GIA. Each frame in Fig. 4 is simply the difference between the associated frames in Figs 6 and 7 (i.e. Fig. 4a =

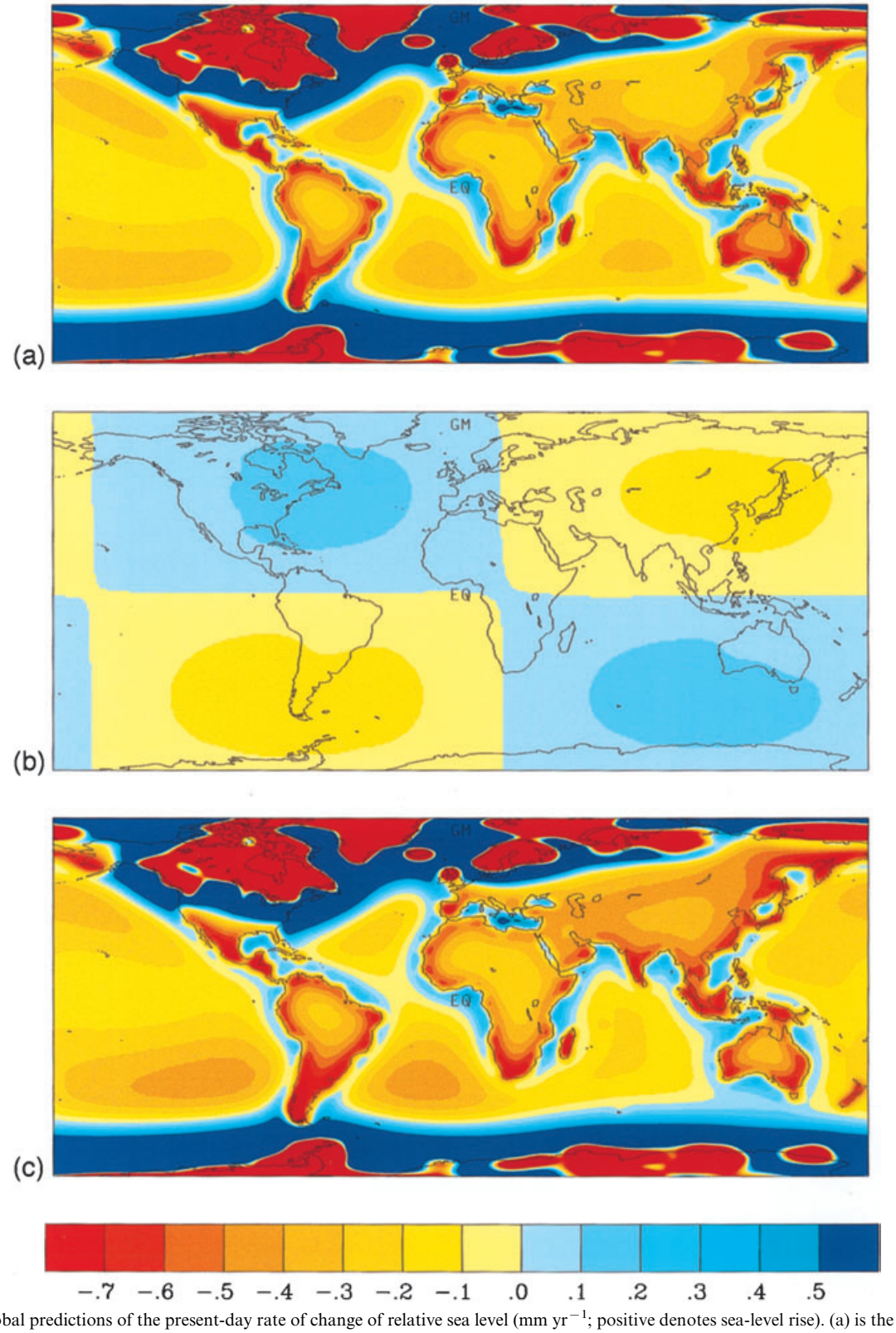

Figure 4. Global predictions of the present-day rate of change of relative sea level (mm yr^{-1}; positive denotes sea-level rise). (a) is the prediction for the case of a non-rotating earth, (b) is the signal due to variations in the Earth's rotation, and (c) is the total signal (i.e. a + b) predicted for a rotating planet. The scale at the bottom of the plot extends from −0.8 to 0.6 mm yr^{-1}. The deep red and blue evident in the near-field (polar) regions of (a) and (c) are off this scale, and in these areas the colours provide only a measure of the geometry of the rebounding regions (red) and subsiding peripheral bulges (blue). The colour scale is chosen so as to encompass the 'rotation' signal and to focus on the pattern of relative sea-level change in the far field, beyond the main peripheral bulges.

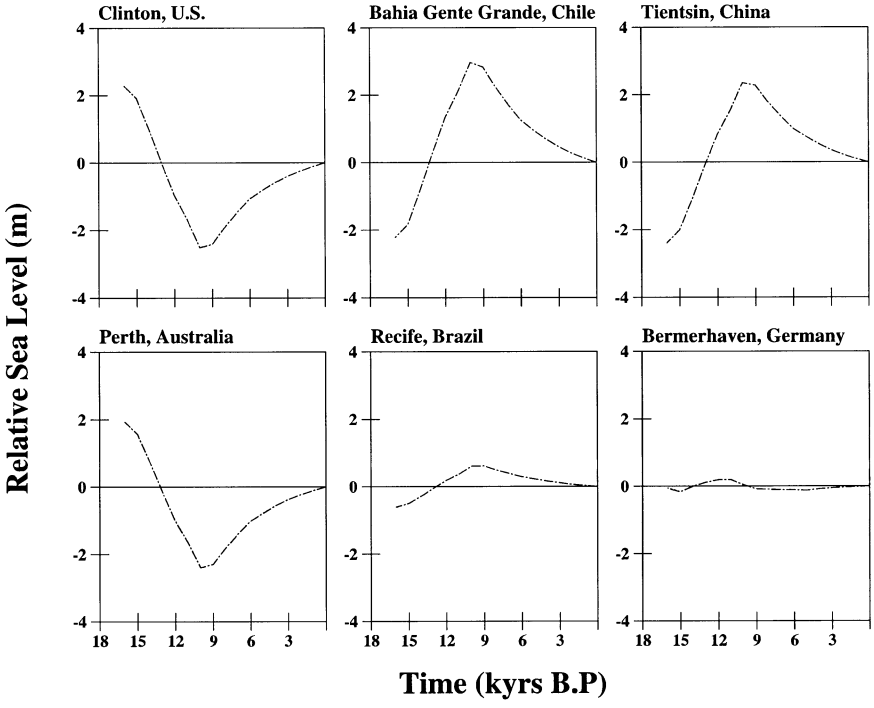

Figure 5. Postglacial RSL variations at six different sites due to rotational effects alone. Predictions are based on the earth and ice models discussed in the text. The dashed and dotted lines, which lie directly on top of each other, are generated using, respectively, the exact expressions (11a)–(11e) for the perturbing rotational potential and the approximate expressions (12a)–(12e).

Fig. 6a–Fig. 7a, etc.) For purposes of comparison, Fig. 8 shows profiles through these various fields along the entire 286°E line of longitude (left-hand side) and the far-field portion of this line (right-hand side).

In the near field, the total RSL signal is dominated by the radial displacement of the solid surface; in constructing Figs 6 and 7, we have reversed the sign of the colour scheme relative to Fig. 4 in order to highlight this similarity [compare Figs 4(a) and 7(a) and also Figs 4(c) and 7(c)]. As we discussed above, within the far-field oceanic regions (that is, away from the effects of continental levering) the geoid subsidence is larger than the (meltwater-induced) solid surface subsidence and an RSL fall ensues.

Since the predicted present-day (north) pole path is in the direction of Hudson Bay (Figs 2 and 3), the rotational driving potential is gradually diminishing in the quadrant that includes the US east coast and Australia. The geoid and solid surface are subsiding in these regions (Figs 6b and 7b, respectively). In fact, the maximum solid surface subsidence rate is ~ 0.54 mm yr^{-1}, while the geoid (or absolute sea level) is falling at ~ 0.41 mm yr^{-1}. Thus, an RSL rise of ~ 0.13 mm yr^{-1} is predicted for these regions (Fig. 4b). The TPW-induced RSL, geoid and radial solid surface responses are of opposite sign in the quadrants including South America and Asia.

These results raise a significant issue. For a purely inviscid planet, the geoid and solid surfaces will deform by the same amount in the presence of a TPW-induced driving potential. In this case, the RSL perturbation associated with the driving potential will be zero. For the viscoelastic model, the geoid and the radial position of the solid surface move in the same sense in response to the TPW-induced driving potential, but with different amplitudes, thus a non-zero RSL perturbation is predicted. Nevertheless, in the viscoelastic case the RSL prediction is significantly smaller (by a factor of 3–4) than the predicted perturbation to either of the RSL bounding surfaces. Indeed, the maximum peak-to-peak radial and geoid displacement rates are ~ 1 mm yr^{-1}.

The perturbation to absolute sea level (geoid) due to the rotational driving potential is more significant when compared to the load-induced perturbation (i.e. the non-rotating case) than the analogous relative sea-level predictions [compare the difference between Figs 4(a) and (c) with the discrepancy between Figs 6(a) and (c)]. Perhaps the most remarkable feature of the geoid predictions is that the rotational feedback is large enough, in the far field, to imprint a significant $Y_{2,1}$ geometry on the total GIA prediction (Fig. 6c). At mid-latitudes, along the lines of longitude 286°E and 106°E, the geoid rates associated with the rotational driving potential are of roughly the same magnitude as the broad geoid subsidence due to syphoning (see Fig. 8). As a consequence, the total predicted geoid rates (Fig. 6c) are nearly zero in parts of Asia and southern South America and are roughly double the values predicted for the non-rotating case in, for example, south-western Australia. The TPW-induced geoid perturbation is also non-negligible within the near field. As an example, the geoid rate in Hudson Bay is reduced, in excess of 20 per cent, by the rotation effect.

TPW-induced effects are also clearly evident in the global map of 'total' GIA-induced radial displacement rates (Fig. 7c). As an example, the uplift of the solid surface in the vicinity of South America due to TPW adds to the 'levering' signal over the continent and also results in a broad area of uplift in the adjacent ocean basins. In contrast, the rotational driving potential has the opposite effect in the vicinity of Australia. We will return to our predictions of radial crustal velocity in the context of a discussion of 3-D surface deformation rates.

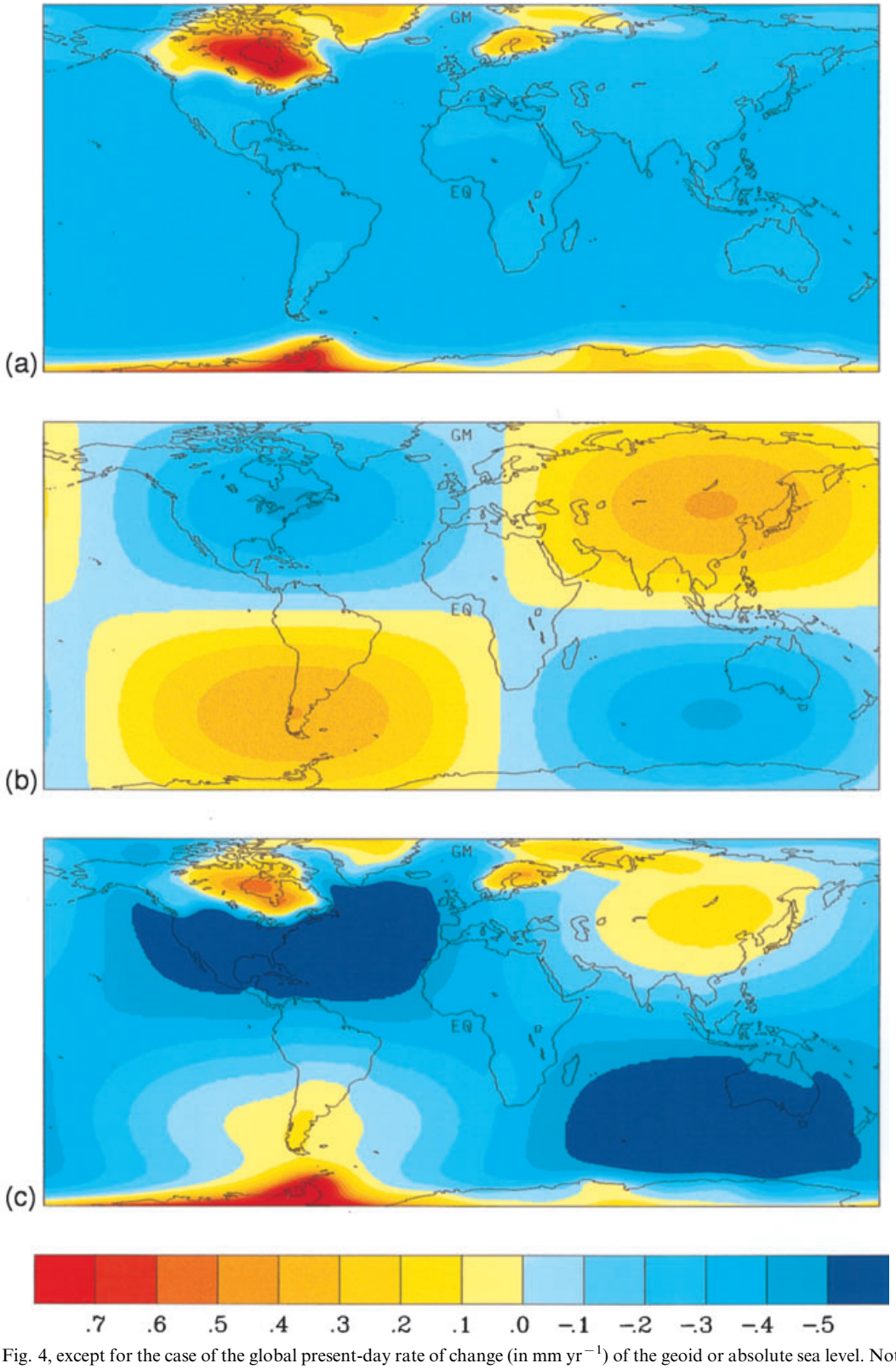

Figure 6. As in Fig. 4, except for the case of the global present-day rate of change (in mm yr^{-1}) of the geoid or absolute sea level. Note the change in sign of the colour bar relative to Fig. 4 (positive denotes an upwarping of the geoid).

Global predictions of GIA-induced present-day rates of change of the geoid and the radial position of the solid surface that include the perturbing effect of rotational feedback were first presented by Peltier (1999). [Analogous predictions for the non-rotating case were first shown by Mitrovica & Peltier (1991).] Peltier (1999) predicted that the rotational effect on radial velocities was small [a comparison of his Figs 11(b) and 12(b) suggests a perturbation of the order of 0.02 mm yr^{-1}]

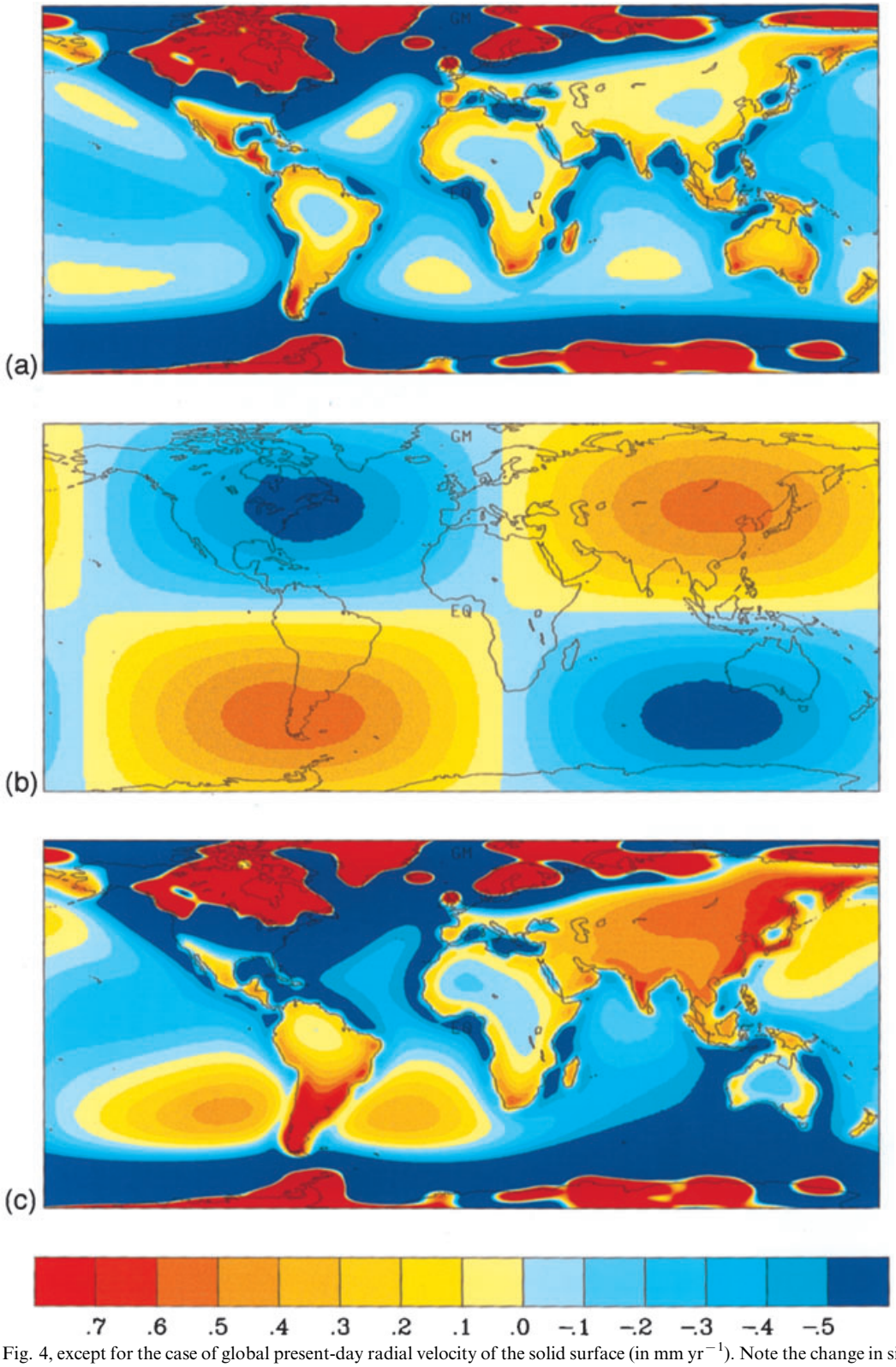

Figure 7. As in Fig. 4, except for the case of global present-day radial velocity of the solid surface (in mm yr^{-1}). Note the change in sign of the colour bar relative to Fig. 4 (positive denotes an uplift of the solid surface). In (a) the localized regions of light yellow in the oceans and light blue in the middle of some continents (e.g. Africa, South America) are somewhat misleading: in each case, the amplitudes of these signals are only marginally different from zero and hence they may be thought of as areas of negligible radial crustal velocities.

and that the TPW-induced perturbation in RSL (which reached a maximum of $\sim$0.2 mm yr^{-1} for the earth and ice models he adopted) arose almost entirely from TPW-induced geoid variations. Indeed, he described these latter two fields as 'identical' (Peltier 1999, p. 121). In contrast, our results suggest that the geoid and solid surfaces move together in response to TPW and that the perturbation to each is significantly larger than suggested by Peltier's (1999) analysis.

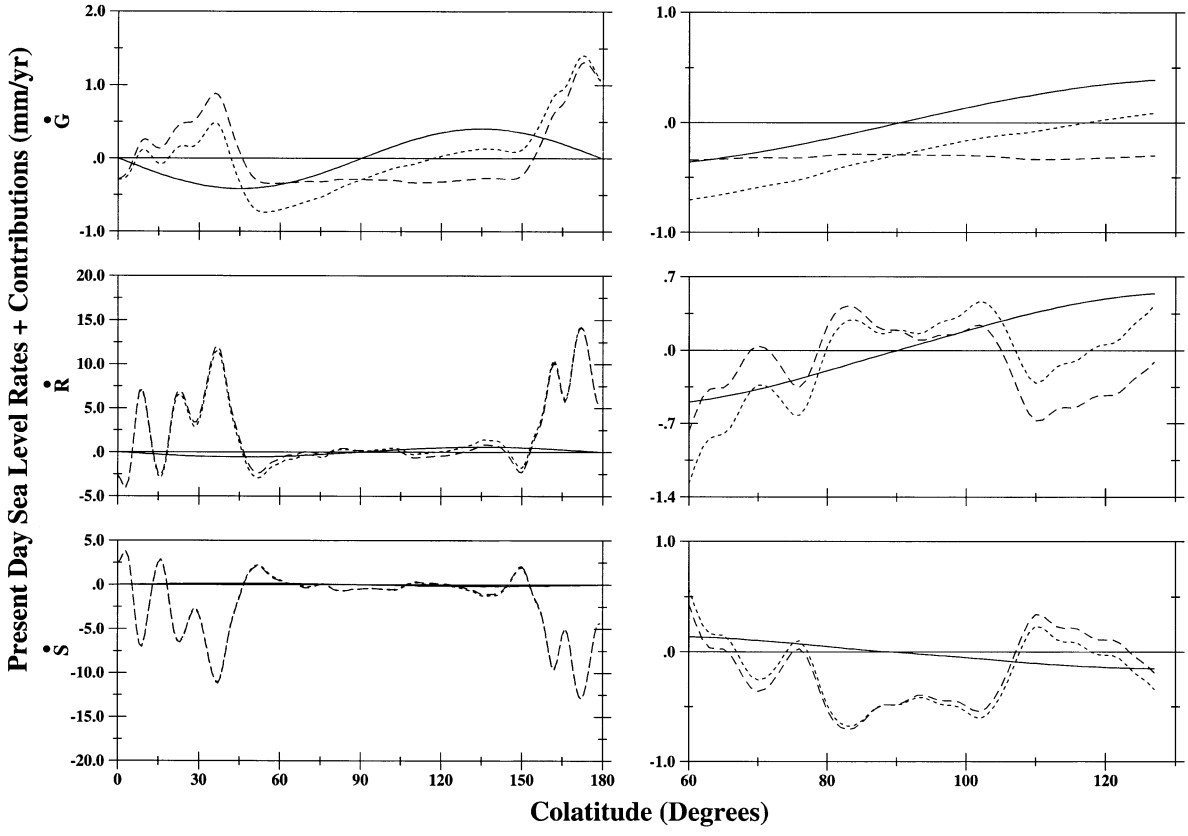

Figure 8. Profiles of present-day rates of change of relative sea-level ($\dot{S}$), geoid or absolute sea level ($\dot{G}$), and the radial position of the solid surface ($\dot{R}$), along the great circle line of longitude 286°E. The left-hand side shows results extending from the north to the south pole, while the right-hand side shows only the segment of the great circle extending from 60° to 130° colatitude. The dashed and dotted lines refer to predictions for the non-rotating and rotating cases, respectively, while the solid line is the signal due to the perturbation in the rotation vector (that is, solid plus dashed equals dotted).

3.1.3 3-D crustal deformation rates

In Fig. 9 we show global maps of predictions of present-day horizontal crustal velocities due to GIA. (a) is the prediction for the non-rotating case, while (b) is the signal associated with the rotational driving potential. The total prediction, (c), is obtained from the vector sum of these two fields. Fig. 9, together with Fig. 7, provides the present-day 3-D crustal velocity field predicted on the basis of the 'test' model. Fig. 10 shows profiles for the three components of velocity along the entire 286°E line of longitude (left-hand side) and the far-field portion of this line (right-hand side).

The general forms of GIA-induced horizontal motions on a non-rotating earth have been discussed in the literature (e.g. James & Lambert 1993; Mitrovica *et al.* 1993, 1994b; Peltier 1998a). In previously glaciated regions, the rebound of the crust is accompanied by outward-directed horizontal motions. Beyond this region, a transition occurs such that the motions become directed towards the centres of glaciation. This produces a broad trend of poleward horizontal rates (north in the Northern Hemisphere and south in the Southern Hemisphere).

The broad pattern of horizontal motions due to the rotational driving potential is easily understood in relation to the analogous radial motions in Fig. 7(b). The horizontal motions are sensitive to the gradient of the radial motions; hence, the horizontal velocities trend towards zero at the centres of the four $Y_{2,1}$ quadrants. That is, the horizontal velocities are small in regions (central Asia, eastern North America, southern South America and southwestern Australia) where the radial velocities are a maximum.

In quadrants of TPW-induced subsidence (e.g. North America, Australia) the sense of the associated horizontal motions is outwards from the point of zero horizontal velocity. In contrast, in quadrants where the TPW produces an uplift (e.g. Asia, southern South America) the horizontal velocities are directed inwards towards the point of zero horizontal velocity. This pattern is intriguing, since it is opposite to the predictions associated with the response of previously glaciated regions to the removal of the surface mass load (see Fig. 9a, where outward horizontal velocities accompany postglacial rebound). The difference is probably linked to the spatial scale of the two processes. The 'outward' horizontal velocity associated with mass load-induced rebound is driven in large part by the bending of the elastic lithosphere. In contrast, the much longer-wavelength (degree two) TPW effect is associated with tractions due to deeper mantle flow (see James 1991 for a detailed discussion of these two processes).

The amplitudes of the horizontal motions associated with the rotational driving potential (which, for our test model, reach in excess of 0.5 mm yr^{-1}) are comparable to the predictions derived using a non-rotating earth within the far field (see Figs 9a and b and the middle rows of Fig. 10). In fact, there are many regions in which the rotational signal dominates the contribution predicted using the usual non-rotating theory

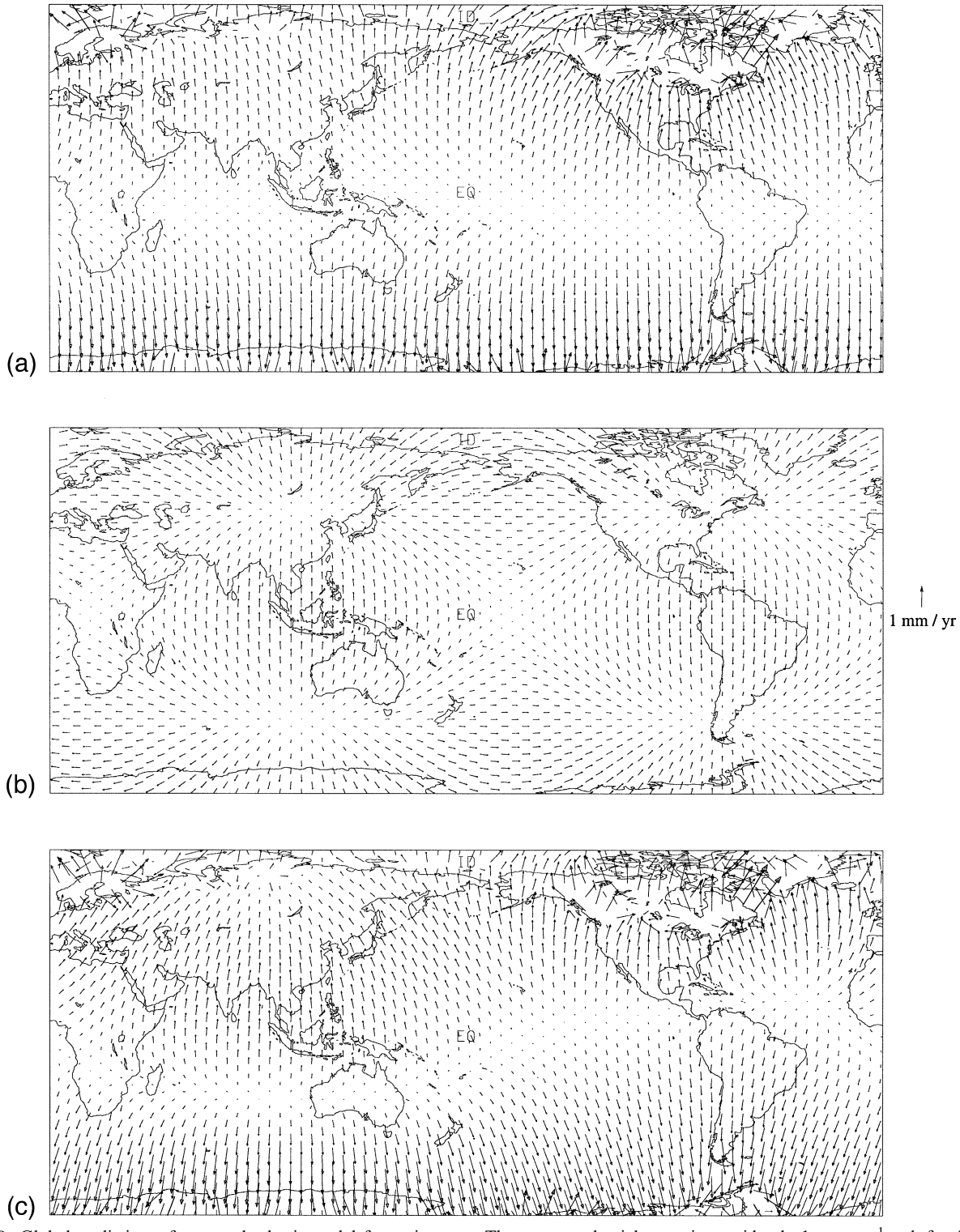

Figure 9. Global predictions of present-day horizontal deformation rates. The arrow on the right margin provides the 1 mm yr^{-1} scale for the vector amplitudes. (a) is the prediction for the case of a non-rotating earth, (b) is the signal due to variations in the Earth's rotation, and (c) is the total signal (i.e. a + b) predicted for a rotating planet. The analogous predictions for present-day radial displacement rates are given in Fig. 7.

(e.g. northern South America, northern Australia, etc.) In the near field, the TPW-induced horizontal motions are generally smaller than the signal associated with the ice loading; however, they clearly cannot be ignored.

To explore this near-field case further, Fig. 11 shows horizontal crustal velocities predicted on the basis of both rotating and non-rotating earth models for two regions where GPS data are currently being obtained to constrain the GIA process, namely, the US east coast (Nerem *et al.* 1997) and Fennoscandia (BIFROST 1996; Milne *et al.* 2001). The predicted TPW effect on horizontal crustal deformations is near-maximum in Fennoscandia (Fig. 9b), while TPW-induced radial velocities

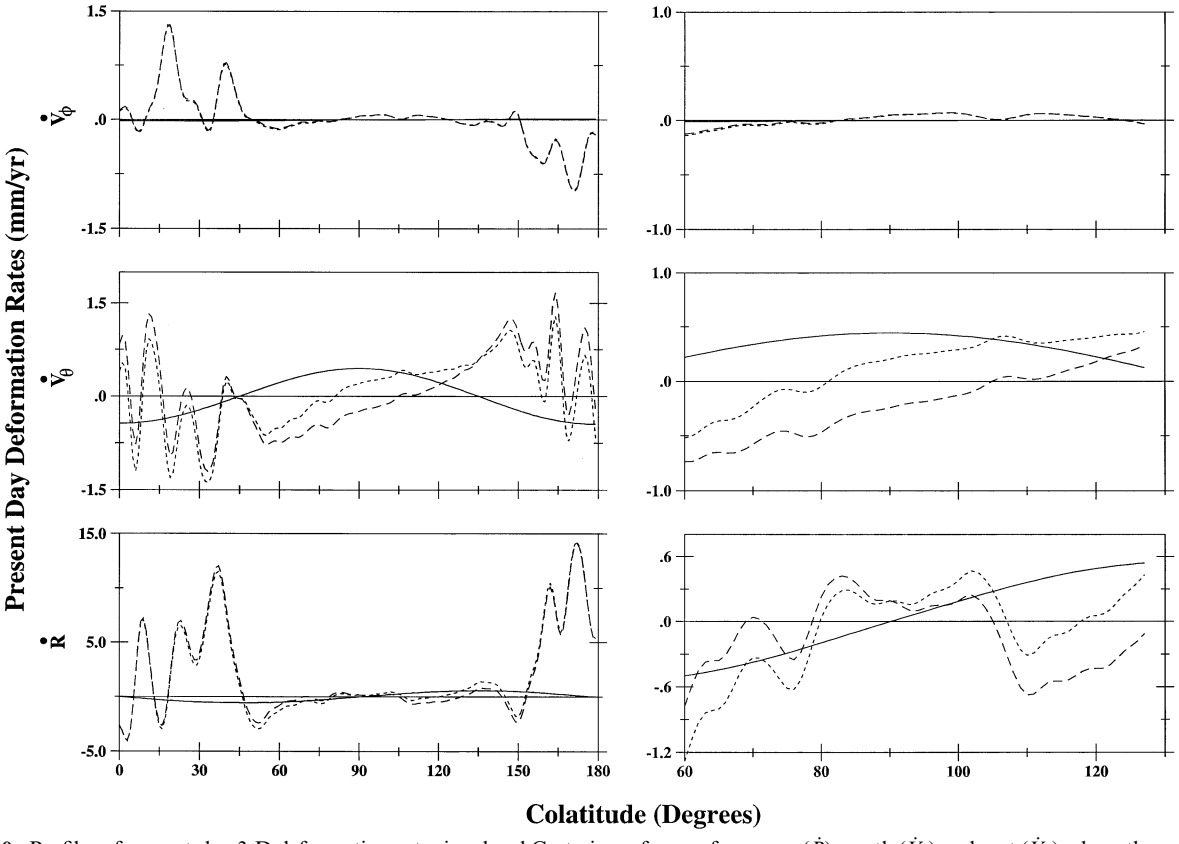

Figure 10. Profiles of present-day 3-D deformation rates in a local Cartesian reference frame: up ($\dot{R}$), south ($\dot{V}_\theta$) and east ($\dot{V}_\phi$), along the great circle line of longitude 286°E. The left-hand side shows results extending from the north to the south pole, while the right-hand side shows only the segment of the great circle extending from 60° to 130° colatitude. The dashed and dotted lines refer to predictions for the non-rotating and rotating cases, respectively, while the solid line is the signal due to the perturbation in the rotation vector (that is, solid plus dashed equals dotted). Gradients in the radial velocity trend roughly north–south along the great circle sampled in this figure (see Fig. 7); accordingly, along these profiles the TPW-induced horizontal velocity vectors are generally dominated by the $\dot{V}_\theta$ component.

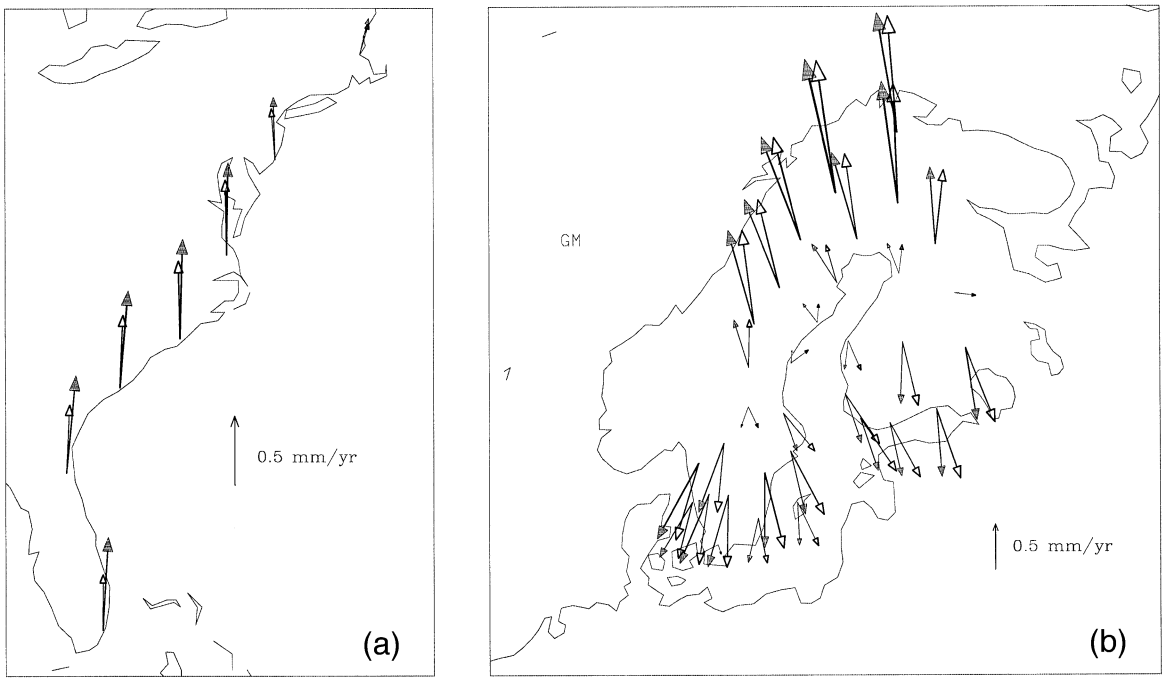

Figure 11. Present-day horizontal deformation rates (a) along the east coast of North America and (b) in Fennoscandia. The vertical arrow at the bottom right within each frame provides a scale for the vector amplitudes. The solid arrowhead represents the prediction for the non-rotating case. The open three-sided arrowhead is the analogous prediction for the rotating case.

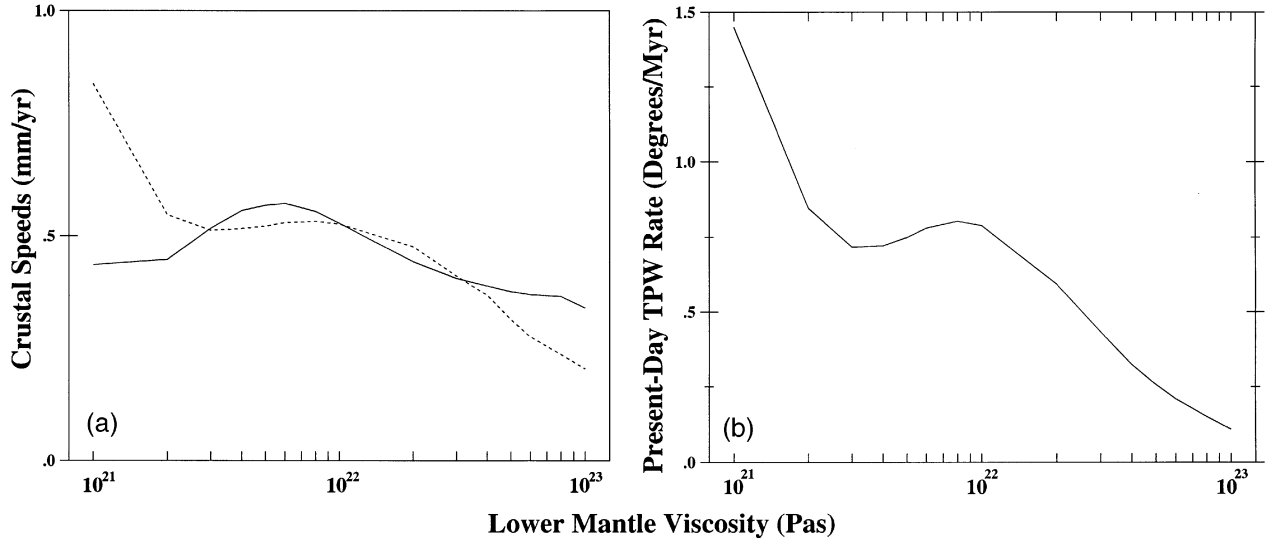

Figure 12. (a) Predictions of the maximum present-day radial (dotted line) and horizontal (solid line) crustal speed due to GIA-induced rotational effects as a function of the lower mantle viscosity of the adopted earth model. (b) Predicted present-day rate of TPW as a function of the lower mantle viscosity. In both frames, the upper mantle viscosity is taken to be 10^{21} Pa s and the lithospheric thickness is 95 km. The ice history is described in the text. The abscissa value of 2×10^{21} Pa s represents the test earth model, also described in the text.

peak within the former region (Fig. 7b). Along the US east coast the horizontal motions due to the surface mass load alone (i.e. the non-rotating case) are directed northwards, while the TPW signal is roughly southwards, hence the main effect of the latter is to reduce the amplitude of the predicted horizontal speeds relative to the non-rotating theory. As we move south along the coast, towards the equator, the TPW feedback increases so that by southern Florida the horizontal speed is reduced by $\sim$40 per cent when the theory that incorporates TPW-induced deformations is adopted. In contrast, over Fennoscandia, the TPW effect is characterized by a broad eastward-directed signal (Fig. 9b) and thus the main effect is a change in the direction of the horizontal motions relative to results generated from the non-rotating theory. We conclude that geodetic constraints on 3-D crustal deformations should be analysed using a GIA methodology extended to incorporate the influence of TPW.

In Fig.12(a) we show predictions of the maximum rotation-induced perturbation to the horizontal (solid line) and radial (dotted line) crustal speeds as a function of the value of $\nu_{\rm lm}$ adopted in the predictions. As an aid to interpreting Fig. 12(a), we also plot the predicted present-day rate of TPW for the same suite of earth models (Fig. 12b). The rather complex non-monotonic relationship evident in Fig. 12(b), first demonstrated by Yuen *et al.* (1986), has recently been analysed in detail by Mitrovica & Milne (1998). In qualitative terms, the TPW rate is roughly constant for lower mantle viscosities in the range 2×10^{21}–10^{22} Pa s. The predicted TPW rate drops rapidly as the lower mantle is stiffened from 10^{21} to 2×10^{21} Pa s and somewhat less rapidly above 10^{22} Pa s.

The radial velocity results in Fig. 12(a) clearly reflect the pattern of present-day TPW rates predicted for the same set of earth models. As an example, the isoviscous mantle model is characterized by the highest present-day TPW rates and radial velocities. On a viscoelastic earth, the rotation-induced response is a function of the complete time history of the forcing, not simply the present-day rate of change of this forcing, so this relationship might not be expected *a priori*. Indeed, the relationship is far less clear for horizontal velocities, particularly for model predictions with $\nu_{\rm lm} < 4 \times 10^{21}$ Pa s. In any event, Fig. 12(a) indicates that TPW-induced crustal deformation rates remain significant over a wide range of earth models.

Finally, we consider how our predictions of the TPW-induced crustal deformations depend on the number of glacial cycles incorporated within the adopted ice mass history. Fig. 13

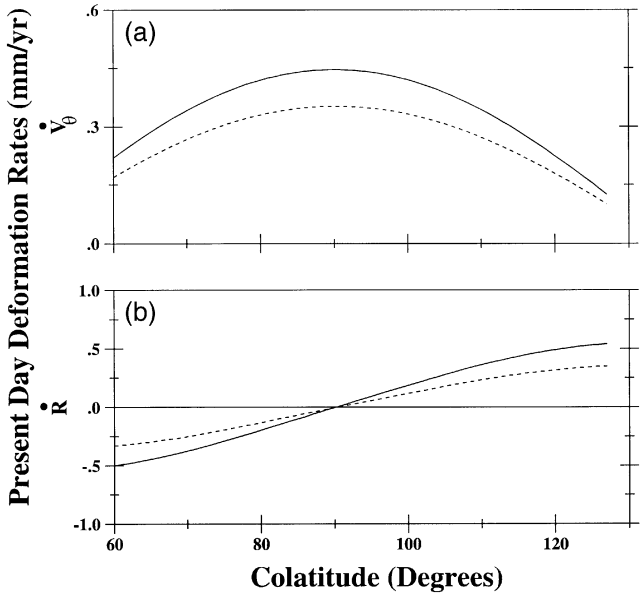

Figure 13. Profiles of predicted present-day crustal deformation rates in a local Cartesian reference frame: up ($\dot{R}$) and south ($\dot{V}_\theta$), along the great circle line of longitude 286°E extending from 60° to 130° colatitude. The predictions only include the response due to the rotational driving potential, and they are based on the test earth model described in the text. The lines are distinguished on the basis of the number of glacial cycles used in constructing the ice history, either eight (solid line) or one (dotted line).

shows predictions of the TPW effect on $\dot{V}_\theta$ and $\dot{R}$ within the far field based on the test earth model and an ice load history characterized by either eight glacial cycles (as in all our previous results) or a single glacial cycle. The eight-cycle calculations adopted in this study are consistent with oxygen isotope records that show that the 100 kyr periodicity of the glacial cycles extends back to $\sim$800 ka (e.g. Hays *et al.* 1976). An assumption of a single glacial cycle yields radial and horizontal velocities that are 40 and 20 per cent lower, respectively, than those based on the more realistic ice load history.

3.2 Rotational feedback on GIA: present-day melting events

Predicting geophysical observables (for example, RSL change, anomalies in the gravitational field and rotational state and 3-D crustal deformations) arising from variations in the mass balance of major polar ice complexes (Greenland, Antarctic) and mountain glaciers has been the subject of considerable recent activity (e.g. Gasperini *et al.* 1986; Peltier 1988; Mitrovica & Peltier 1993; Wahr *et al.* 1995; James & Ivins 1997; Johnston & Lambeck 1999; Mitrovica *et al.* 2001). These predictions have not generally incorporated rotational feedback into the forward analyses, and to complete this study we address this problem using the theoretical formalism described above.

The present-day mass balance of the Greenland and Antarctic ice complexes remains highly uncertain. Accordingly, we treated the simple case where each of these ice complexes is subject to a geographically uniform melting event with a rate equivalent to 1 mm yr^{-1} of global eustatic sea-level rise. The response to mass variations of different amplitude (and even different sign) can be generated by simply scaling the predictions described below appropriately. In addition, we also predicted TPW-induced signals associated with the melting of 31 small ice sheets and mountain glaciers tabulated by Meier (1984). These melting events account for an equivalent eustatic sea-level rise of $\sim$0.4 mm yr^{-1}. In each case (polar ice complexes, mountain glaciers), we computed a gravitationally self-consistent ocean meltwater load. The timescale of the melting is sufficiently rapid that the Earth's response is primarily elastic, hence the predictions described below are insensitive to the adopted radial profile of mantle viscosity or lithospheric thickness.

Fig. 14 shows global predictions of the present-day rate of change of (a) relative sea level, (b) the geoid and (c) the radial position of the solid surface, due to the perturbation in rotation alone, arising from the model Greenland melting scenario. A global prediction of the total sea-level rate for the same melting scenario is given elsewhere (Mitrovica *et al.* 2001). In this calculation, the north rotation pole is predicted to move towards Greenland along the line 320°E and thus the orientation of the dominant $Y_{2,1}$ geometry in Fig. 14 is slightly different from that evident in our earlier GIA predictions (e.g. Figs 4, 6 and 7). As an example, the North Atlantic is now a site of peak TPW-induced signals. At this location, the relative sea level, the geoid and the radial position of the solid surface are perturbed -0.14, -0.23 and -0.09 mm yr^{-1}, respectively. In contrast to the GIA predictions of the last section, the RSL response due to present-day melting of the Greenland ice complex is therefore dominated by the geoid warping rather than by the radial velocity of the solid surface. Although the latter two fields still track each other, the subsidence rate of the geoid is greater than that of the solid surface in the northern Atlantic, and the result is an RSL fall within this region. In any event, the TPW-induced signal contributes significantly to the total departure of both RSL and the sea surface (geoid) from a simple eustatic (i.e. geographically uniform) meltwater redistribution. Indeed, the rotational perturbing potential alone drives a departure from eustasy of roughly 28 and 46 per cent (peak-to-peak) for relative and absolute sea level, respectively.

TPW-induced sea level and radial crustal velocities driven by either our simple Antarctic ice melting scenario or Meier's (1984) sources are significantly smaller than the signals evident in Fig. 14. Antarctic melting events, since they are centred near the south pole, will clearly be less efficient at driving TPW than equivalent variations in the mass balance of Greenland ice. Furthermore, since Meier's (1984) sources are rather widely distributed, they are also not as efficient at driving TPW as a coherent Greenland melting event of equivalent mass flux. Finally, we also calculated horizontal crustal velocities for the present-day melting scenarios and we found that TPW-induced effects are small (less than 0.1 mm yr^{-1}).

4 FINAL REMARKS

Geodetic constraints are increasingly being brought to bear on a classic problem in geophysics, namely the response of the Earth to loading associated with the Late Pleistocene glacial cycles. Indeed, GIA is a central issue in ongoing or planned geodetic surveys, for example the BIFROST GPS effort (BIFROST 1996; Milne *et al.* 2001) and the GRACE satellite gravity mission (Bentley & Wahr 1998). This focus stems from two related applications. First, observations of ongoing GIA provide a powerful database for constraining mantle viscosity and Late Pleistocene ice history. Second, geodetic constraints on climate change observables, for example gravity and sea-level anomalies arising from variations in the mass balance of polar ice complexes, will be contaminated by a large and uncertain GIA contribution.

As geodetic constraints become more accurate, the theoretical and numerical framework for predicting GIA observables will continue to be refined. This study has focused, in large part, on one potentially important issue in this refinement, specifically the feedback of GIA-induced perturbations in Earth rotation on geodetically relevant geophysical observables. We have extended and completed previous work to consider a suite of such observables, including 3-D crustal velocities and relative and absolute sea-level variations. We have concluded that the feedback will, in general, need to be incorporated into analyses of geodetic data. As an example, TPW-induced 3-D crustal velocities can exceed 0.5 mm yr^{-1}, and are thus larger than the quoted uncertainty of a number of GPS surveys, including BIFROST.

We have also demonstrated that TPW driven by any ongoing mass flux from the Greenland ice sheet is capable of significantly perturbing the pattern of global sea-level rise that would be associated with the melting event. It is commonly assumed that melting of polar ice sheets induced, for example, by climate warming yields a nearly eustatic trend in sea level, although it has long been recognized that self-gravitation and loading

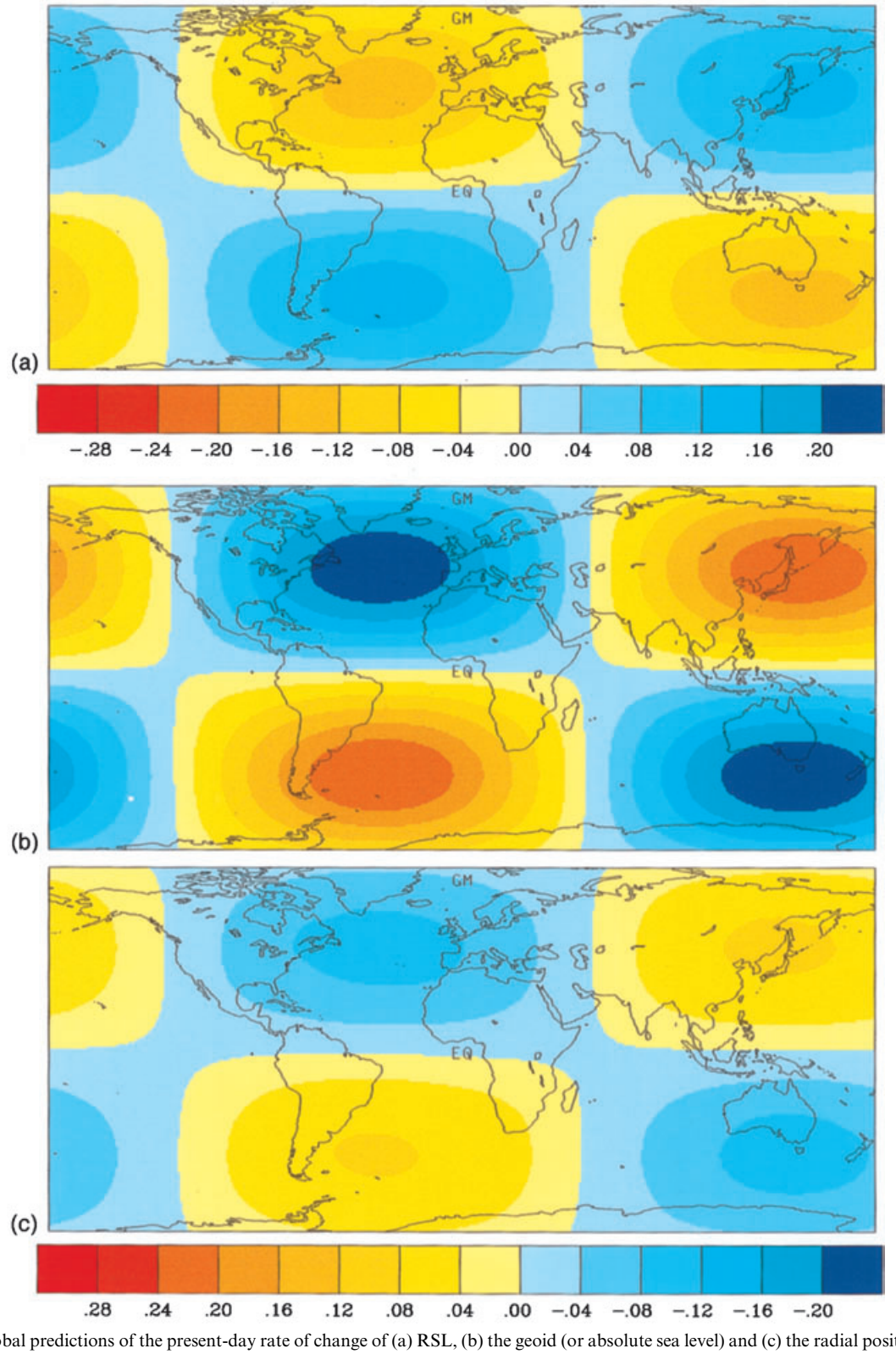

Figure 14. Global predictions of the present-day rate of change of (a) RSL, (b) the geoid (or absolute sea level) and (c) the radial position of the solid surface due to the rotational driving potential alone for the case of the simple Greenland ice melting scenario described in the text.

effects will lead to significant departures from eustasy (e.g. Woodward 1888; Farrell & Clark 1976; Mitrovica *et al.* 2001; Plag & Jüttner 2001). We have found that the rotation effect alone is capable of producing a significant departure from eustasy and this demonstration has fundamental implications for the interpretation of both tide gauge constraints on RSL and satellite altimetry of the sea-surface height (Mitrovica *et al.* 2001; Tamisiea *et al.* 2001).

ACKNOWLEDGMENTS

We than Bert Vermeersen for his constructive review of the manuscript. This research was funded by NSERC, the Royal Society of Great Britain, NASA grants NAG5-1930 and NAG5-6068 and the Smithsonian Institution.

REFERENCES

Bentley, C.R. & Wahr, J.M., 1998. Satellite gravity and the mass balance of the Antarctic ice sheet, *J. Glaciol.,* **44,** 207–213.

BIFROST Project Members, 1996. GPS measurements to constrain geodynamic processes in Fennoscandia, *EOS, Trans. Am. geophys. Un.,* **77,** 337–341.

Bills, B.G., 1995. Solid earth interaction with glacial cycle mass loads, *EOS, Trans. Am. geophys. Un.,* **76**(46), 159.

Bills, B.G. & James, T.S., 1996. Late Quaternary variations in relative sea level due to glacial cycle polar wander, *Geophys. Res. Lett.,* **23,** 3023–3026.

Clark, J.A., Farrell, W.E. & Peltier, W.R., 1978. Global changes in postglacial sea level: a numerical calculation, *Quat. Res.,* **9,** 265–287.

Dziewonski, A.M. & Anderson, D.L., 1981. Preliminary reference earth model (PREM), *Phys. Earth planet. Inter.,* **25,** 297–356.

Farrell, W.E. & Clark, J.A., 1976. On postglacial sea level, *Geophys. J. R. astr. Soc.,* **46,** 647–667.

Gasperini, P., Sabadini, R. & Yuen, D.A., 1986. Excitation of the Earth's rotational axis by recent glacial discharges, *Geophys. Res. Lett.,* **13,** 533–536.

Han, D. & Wahr, J., 1989. Post-glacial rebound analysis for a rotating Earth, in *Slow Deformations and Transmission of Stress in the Earth*, eds Cohen, S. & Vanicek, P. *AGU Monogr. Ser.,* **49,** 1–6.

Hays, J.D., Imbrie, J. & Shackleton, N.J., 1976. Variations in the Earth's orbit: pacemaker of the ice ages, *Science,* **194,** 1121–1132.

Heiskanen, W.A. & Vening Meinesz, F.A., 1958. *The Earth and its Gravity Field,* McGraw-Hill, New York.

James, T.S., 1991. Post-glacial deformation, *PhD thesis,* Princeton University, Princeton, NJ.

James, T.S. & Ivins, E.R., 1997. Global geodetic signatures of the Antarctic ice sheet, *J. geophys. Res.,* **102,** 605–633.

James, T.S. & Lambert, A., 1993. A comparison of VLBI data with the ICE-3G glacial rebound model, *Geophys. Res. Lett.,* **20,** 871–874.

Johnston, P., 1993. The effect of spatially non-uniform water loads on predictions of sea level change, *Geophys. J. Int.,* **114,** 615–634.

Johnston, P. & Lambeck, K., 1999. Postglacial rebound and sea level contributions to changes in the geoid and the Earth's rotation axis, *Geophys. J. Int.,* **136,** 537–558.

Lambeck, K., 1980. *The Earth's Variable Rotation,* Cambridge University Press, Cambridge.

Meier, M.F., 1984. Contribution of small glaciers to global sea level, *Science,* **226,** 1418–1421.

Miller, S.P. & Wunsch, C., 1973. The pole tide, *Nature,* **246,** 98–102.

Milne, G.A. & Mitrovica, J.X., 1996. Postglacial sea-level change on a rotating Earth: first results from a gravitationally self-consistent sea-level equation, *Geophys. J. Int.,* **126,** F13–F20.

Milne, G.A. & Mitrovica, J.X., 1998. Postglacial sea-level change on a rotating Earth, *Geophys. J. Int.,* **133,** 1–10.

Milne, G.A., Davis, J.L., Mitrovica, J.X., Scherneck, H.-G., Johansson, J.M., Vermeer, M. & Koivula, H., 2001. Space-geodetic constraints on glacial isostatic adjustment in Fennoscandia, *Science,* **291,** 2381–2385.

Mitrovica, J.X. & Milne, G.A., 1998. Glaciation-induced perturbations in the Earth's rotation: a new appraisal, *J. geophys. Res.,* **103,** 985–1005.

Mitrovica, J.X. & Peltier, W.R., 1991. On post-glacial geoid subsidence over the equatorial oceans, *J. geophys. Res.,* **96,** 20 053–20 071.

Mitrovica, J.X. & Peltier, W.R., 1993. Present-day secular variations in the zonal harmonics of the Earth's geopotential, *J. geophys. Res.,* **98,** 4509–4526.

Mitrovica, J.X., Davis, J.L. & Shapiro, I.I., 1993. Constraining proposed combinations of ice history and Earth rheology using VLBI determined baseline length rates in North America, *Geophys. Res. Lett.,* **20,** 2387–2390.

Mitrovica, J.X., Davis, J.L. & Shapiro, I.I., 1994a. A spectral formalism for computing three-dimensional deformations due to surface loads, 1. Theory, *J. geophys. Res.,* **99,** 7057–7073.

Mitrovica, J.X., Davis, J.L. & Shapiro, I.I., 1994b. A spectral formalism for computing three-dimensional deformations due to surface loads, 2. Present-day glacial isostatic adjustment, *J. geophys. Res.,* **99,** 7075–7101.

Mitrovica, J.X., Tamisiea, M.E., Davis, J.L. & Milne, G.A., 2001. Recent mass balance of polar ice sheets inferred from patterns of global sea-level change, *Nature,* **409,** 1026–1029.

Mound, J. & Mitrovica, J.X., 1998. True polar wander as a mechanism for second-order sea level cycles, *Science,* **279,** 534–537.

Munk, W.H. & MacDonald, G.J.F., 1960. *The Rotation of the Earth,* Cambridge University Press, New York.

Nakada, M. & Lambeck, K., 1989. Late Pleistocene and Holocene sea-level change in the Australian region and mantle rheology, *Geophys. J. Int.,* **96,** 497–517.

Nakiboglu, S.M. & Lambeck, K., 1980. Deglaciation effects upon the rotation of the Earth, *Geophys. J. R. astr. Soc.,* **62,** 49–58.

Nerem, R.S., Park, K.D., van Dam, T.M., Schenewerk, M.S., Davis, J.L. & Mitrovica, J.X., 1997. A study of sea level change in the northeastern U.S. using GPS and tide gauge data, *EOS, Trans. Am. geophys. Un.,* **78**(46), 140–141.

O'Connell, R.J., 1971. Pleistocene glaciation and the viscosity of the lower mantle, *Geophys. J. R. astr. Soc.,* **23,** 299–327.

Peltier, W.R., 1974. The impulse response of a Maxwell Earth, *Rev. Geophys.,* **12,** 649–669.

Peltier, W.R., 1976. Glacial isostatic adjustment, II. The inverse problem, *Geophys. J. R. astr. Soc.,* **46,** 669–706.

Peltier, W.R., 1988. Global sea level and earth rotation, *Science,* **240,** 895–901.

Peltier, W.R., 1997. Geoid height time dependence due to glacial isostatic adjustment, *EOS, Trans. Am. geophys. Un.,* **78**(46), 163.

Peltier, W.R., 1998a. Postglacial variations in the level of the sea: implications for climate dynamics and solid-Earth geophysics, *Rev. Geophys.,* **36,** 603–689.

Peltier, W.R., 1998b. Global glacial isostasy and relative sea level: implications for solid Earth geophysics and climate system dynamics, in *Dynamics of the Ice Age Earth: A Modern Perspective*, pp. 17–53, ed. Wu, P., Trans Tech, Zurich, Switzerland.

Peltier, W.R., 1998c. The inverse problem for mantle viscosity, *Inverse Problems,* **14,** 441–478.

Peltier, W.R., 1999. Global sea level rise and glacial isostatic adjustment, *Global planet. Change,* **20,** 93–123.

Plag, H.-P. & Jüttner, H.-U., 2001. Inversion of global tide gauges for present-day ice-load changes, *Proc. 2nd Int. Symp. Environ. Res. in the Arctic.*

Sabadini, R. & Peltier, W.R., 1981. Pleistocene deglaciation and the Earth's rotation: implications for mantle viscosity, *Geophys. J. R. astr. Soc.,* **66,** 553–578.

Sabadini, R. & Vermeersen, L.L.A., 1997. Ice-age cycles: Earth's rotation instabilities and sea-level changes, *Geophys. Res. Lett.,* **24,** 3041–3044.

Sabadini, R., Yuen, D.A. & Boschi, E., 1982. Polar wander and the forced responses of a rotating, multilayered, viscoelastic planet, *J. geophys. Res.,* **87,** 2885–2903.

Sabadini, R., Yuen, D.A. & Boschi, E., 1984. A comparison of the complete and truncated versions of the polar wander equations, *J. geophys. Res.,* **89,** 7609–7620.

Sabadini, R.,Doglioni, C. & Yuen, D.A., 1990. Eustatic sea level fluctuations induced by polar wander, *Nature,* **345,** 708–709.

Tamisiea, M., Mitrovica, J.X., Milne, G.A. & Davis, J.L., 2001. Global geoid and sea-level changes due to present-day ice mass fluctuations: implications for space-geodetic measurements and tide gauge analyses, *J. geophys. Res.,* in press.

Tushingham, A.M. & Peltier, W.R., 1991. ICE-3G: a new global model of late Pleistocene deglaciation based on geophysical predictions of post-glacial relative sea level change, *J. geophys. Res.,* **96,** 4497–4523.

Vermeersen, L.L.A. & Sabadini, R., 1996. Significance of the fundamental mantle relaxation mode in polar wander simulations, *Geophys. J. Int.,* **127,** F5–F9.

Vermeersen, L.L.A., Fournier, A. & Sabadini, R., 1997. Changes in rotation induced by Pleistocene ice masses with stratified analytical Earth models, *J. geophys. Res.,* **102,** 27 689–27 702.

Wahr, J.M., 1985. Deformation induced by polar motion, *J. geophys. Res.,* **90,** 9363–9368.

Wahr, J.M., Han, D. & Trupin, A., 1995. Predictions of vertical uplift caused by changing polar ice volumes on a viscoelastic Earth, *Geophys. Res. Lett.,* **22,** 977–980.

Woodward, R.S., 1888. On the form and position of mean sea level, *USGS Bull.,* **48,** 87–170.

Wu, P., 1978. The response of a Maxwell earth to applied surface mass loads: glacial isostatic adjustment, *MSc thesis,* University of Toronto, Toronto.

Wu, P. & Peltier, W.R., 1984. Pleistocene deglaciation and the Earth's rotation: a new analysis, *Geophys. J. R. astr. Soc.,* **76,** 753–792.

Yuen, D.A. & Sabadini, R., 1985. Viscosity stratification of the lower mantle as inferred from the $\dot{J}_2$ observation, *Ann. Geophys.,* **3,** 647–654.

Yuen, D.A., Sabadini, R. & Boschi, E., 1982. Viscosity of the lower mantle as inferred from rotational data, *J. geophys. Res.,* **87,** 10 745–10 762.

Yuen, D.A., Sabadini, R., Gasperini, P. & Boschi, E., 1986. On transient rheology and glacial isostasy, *J. geophys. Res.,* **91,** 11 420–11 438.

APPENDIX A: TITLE?

The (surface mass load) impulse response of a Maxwell viscoelastic earth model may be expressed in terms of the so-called viscoelastic surface load Love numbers (Peltier 1974). In the time domain, these Love numbers have the form (Peltier 1976)

$$h_\ell^{\mathrm{L}}(t) = h_\ell^{\mathrm{L,E}}\delta(t) + \sum_{j=1}^{J} r_j^{\ell,\mathrm{L}} \exp(-s_j^\ell t)\,, \tag{A1}$$

$$l_\ell^{\mathrm{L}}(t) = l_\ell^{\mathrm{L,E}}\delta(t) + \sum_{j=1}^{J} r'^{\ell,\mathrm{L}}_j \exp(-s_j^\ell t) \tag{A2}$$

and

$$k_\ell^{\mathrm{L}}(t) = k_\ell^{\mathrm{L,E}}\delta(t) + \sum_{j=1}^{J} r''^{\ell,\mathrm{L}}_j \exp(-s_j^\ell t)\,. \tag{A3}$$

The first term on the right-hand sides of these equations is the instantaneous elastic response, while the second term, comprising a set of J 'normal modes', is the non-elastic response. The h, l and k Love numbers are associated with radial displacement, tangential displacement and gravitational potential perturbations, respectively, due to the degree ℓ component of the surface mass point load.

Forms analogous to eqs (A1)–(A3) can also be introduced to describe the response of the viscoelastic earth model to a potential, rather than surface mass, forcing. The viscoelastic tidal Love numbers can be written as

$$h_\ell^{\mathrm{T}}(t) = h_\ell^{\mathrm{T,E}}\delta(t) + \sum_{j=1}^{J} r_j^{\ell,\mathrm{T}} \exp(-s_j^\ell t)\,, \tag{A4}$$

$$l_\ell^{\mathrm{T}}(t) = l_\ell^{\mathrm{T,E}}\delta(t) + \sum_{j=1}^{J} r'^{\ell,\mathrm{T}}_j \exp(-s_j^\ell t) \tag{A5}$$

and

$$k_\ell^{\mathrm{T}}(t) = k_\ell^{\mathrm{T,E}}\delta(t) + \sum_{j=1}^{J} r''^{\ell,\mathrm{T}}_j \exp(-s_j^\ell t)\,. \tag{A6}$$

We adopt the procedure outlined by Peltier (1974) and Wu (1978) to compute the various parameters associated with the surface load and tidal Love numbers for a specified viscoelastic model. Once computed, these parameters can be combined to generate the time-dependent forms Γ^{T}, Γ^{L}, Υ^{T}, Υ^{L}, Φ^{T} and Φ^{L} required in eqs (5)–(7). In particular, we can extend the work of Mitrovica *et al.* (1994a) and Milne & Mitrovica (1998) to write

$$\Gamma_\ell^{\mathrm{T}}(t) = h_\ell^{\mathrm{T,E}}\delta(t) + \sum_{j=1}^{J} r_j^{\ell,\mathrm{T}} \exp(-s_j^\ell t)\,, \tag{A7}$$

$$\Gamma_\ell^{\mathrm{L}}(t) = h_\ell^{\mathrm{L,E}}\delta(t) + \sum_{j=1}^{J} r_j^{\ell,\mathrm{L}} \exp(-s_j^\ell t)\,, \tag{A8}$$

$$\Upsilon_\ell^{\mathrm{T}}(t) = l_\ell^{\mathrm{T,E}}\delta(t) + \sum_{j=1}^{J} r'^{\ell,\mathrm{T}}_j \exp(-s_j^\ell t)\,, \tag{A9}$$

$$\Upsilon_\ell^{\mathrm{L}}(t) = l_\ell^{\mathrm{L,E}}\delta(t) + \sum_{j=1}^{J} r'^{\ell,\mathrm{L}}_j \exp(-s_j^\ell t)\,,$$

$$\Phi_\ell^{\mathrm{T}}(t) = (1 + k_\ell^{\mathrm{T,E}})\delta(t) + \sum_{j=1}^{J} r''^{\ell,\mathrm{T}}_j \exp(-s_j^\ell t) \tag{A11}$$

and

$$\Phi_\ell^{\mathrm{L}}(t) = (1 + k_\ell^{\mathrm{L,E}})\delta(t) + \sum_{j=1}^{J} r''^{\ell,\mathrm{L}}_j \exp(-s_j^\ell t)\,. \tag{A12}$$

Formally, Γ_ℓ, Υ_ℓ and Φ_ℓ are coefficients in Legendre polynomial expansions for Green functions associated with radial displacement, horizontal displacement and the geoid anomaly, respectively.